X-SHAPED AND Y-SHAPED ANDREEV RESONANCE PROFILES IN A SUPERCONDUCTING QUANTUM DOT

Shuo Mi, D. I. Pikulin, M. Marciani, C. W. J. Beenakker[*]

Instituut-Lorentz, Universiteit Leiden, P.O. Box 9506
2300, RA Leiden, The Netherlands

The quasi-bound states of a superconducting quantum dot that is weakly coupled to a normal metal appear as resonances in the Andreev reflection probability, measured via the differential conductance. We study the evolution of these Andreev resonances when an external parameter (such as the magnetic field or gate voltage) is varied, using a random-matrix model for the $N \times N$ scattering matrix. We contrast the two ensembles with broken time-reversal symmetry, in the presence or absence of spinrotation symmetry (class C or D). The poles of the scattering matrix in the complex plane, encoding the center and width of the resonance, are repelled from the imaginary axis in class C. In class D, in contrast, a number $\propto \sqrt{N}$ of the poles has zero real part. The corresponding Andreev resonances are pinned to the middle of the gap and produce a zero-bias conductance peak that does not split over a range of parameter values (Y-shaped profile), unlike the usual conductance peaks that merge and then immediately split (X-shaped profile).

Contribution for the JETP special issue in honor of A. F. Andreev's 75th birthday

1. INTRODUCTION

Half a century has passed since Alexander Andreev reported the curious retro-reflection of electrons at the interface between a normal metal and a superconductor [1]. One reason why Andreev reflection is still very much a topic of active research is the recent interest in Majorana zero modes [2]: nondegenerate bound states at the Fermi level ($E = 0$) consisting of a coherent superposition of electrons and holes, coupled via Andreev reflection. These are observed in the differential conductance as a resonant peak around zero bias voltage V that does not split upon variation of a magnetic field B [3–6]. In the (B, V) plane, the conductance peaks trace out an unusual Y-shaped profile, distinct from the more common X-shaped profile of peaks that meet and immediately split again (see Fig. 1).

It is tempting to think that the absence of a splitting of the zero-bias conductance peak demonstrates that the quasi-bound state is nondegenerate, and hence Majorana. This is mistaken. As shown in a computer simulation [7], the Y-shaped conductance pro-

file is generic for superconductors with broken spin-rotation and broken time-reversal symmetry, irrespective of the presence or absence of Majorana zero modes. The theoretical analysis in Ref. [7] focused on the ensemble-averaged conductance peak, in the context of the weak antilocalization effect [8–11]. Here, we analyze the sample-specific conductance profile, by relating the X-shape and Y-shape to different configurations of poles of the scattering matrix in the complex energy plane [12].
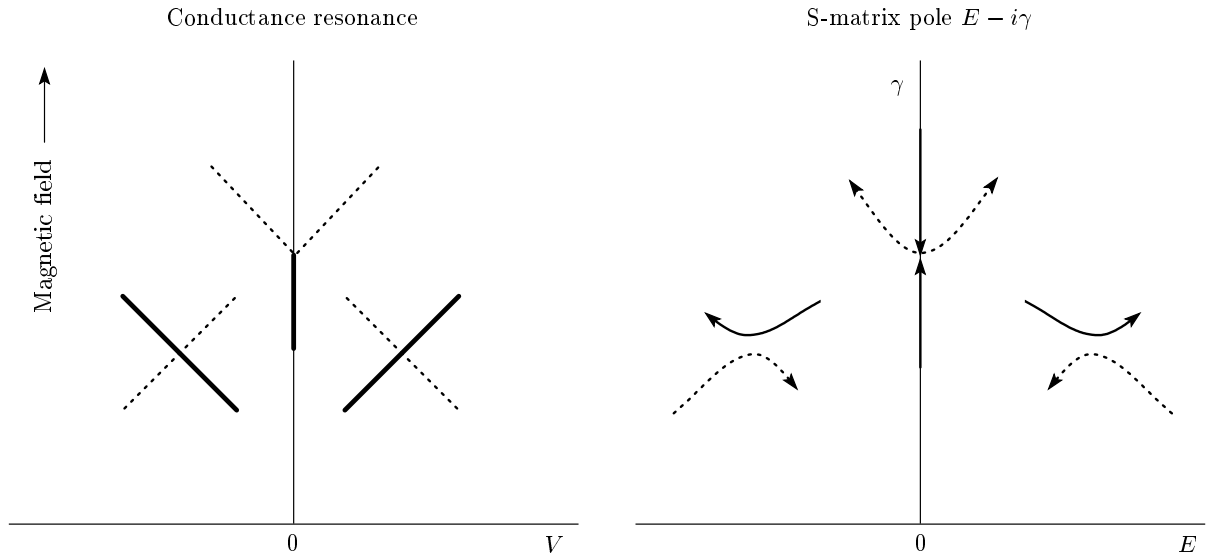
2. ANDREEV BILLIARD

2.1. Scattering resonances

We study the Andreev billiard geometry shown in Fig. 2: a semiconductor quantum dot strongly coupled to a superconductor and weakly coupled to a normal metal. In the presence of time-reversal symmetry, an excitation gap is induced in the quantum dot by the proximity effect [13]. We assume that the gap is closed by a sufficiently strong magnetic field. Quasi-bound states can then appear near the Fermi level ($E = 0$), described by the Hamiltonian

$$\mathcal{H} = \sum_{\mu,\nu} |\mu\rangle H_{\mu\nu} \langle\nu| + \sum_{\mu,a} \left(|\mu\rangle W_{\mu a} \langle a| + |a\rangle W_{\mu a}^* \langle\mu| \right). \quad (1)$$

[*]E-mail: beenakker@lorentz.leidenuniv.nl

Conductance resonance

S-matrix pole $E - i\gamma$

Fig. 1. Left panel: Magnetic field B-dependence of peaks in the differential conductance $G = dI/dV$. The peak positions trace out an X-shaped or Y-shaped profile in the (B, V) plane. Right panel: Location of the poles of the scattering matrix $S(\varepsilon)$ in the complex energy plane $\varepsilon = E - i\gamma$. The arrows indicate how the poles move with increasing magnetic field

The bound states in the closed quantum dot are eigenvalues of the $M \times M$ Hermitian matrix $H = H^\dagger$. The $M \times N$ matrix W couples the basis states $|\mu\rangle$ in the quantum dot to the normal metal, via N propagating modes $|a\rangle$ through a point contact. In principle, we should take the limit $M \to \infty$, but in practice $M \gg N$ suffices.

The amplitudes of incoming and outgoing modes in the point contact at an energy E (relative to the Fermi level) are related by the $N \times N$ scattering matrix [14, 15]

$$S(E) = 1 + 2\pi i W^\dagger \left(H - i\pi W W^\dagger - E\right)^{-1} W. \quad (2)$$

This is a unitary matrix, $S(E)S^\dagger(E) = 1$.

A scattering resonance corresponds to a pole $\varepsilon = E - i\gamma$ of the scattering matrix in the complex energy plane, which is an eigenvalue of the non-Hermitian matrix

$$H_{eff} = H - i\pi W W^\dagger. \quad (3)$$

The positive definiteness of $WW^\dagger$ ensures that the poles all lie in the lower half of the complex plane, $\gamma \geq 0$, as required by causality. Particle–hole symmetry implies that ε and $-\varepsilon^*$ are both eigenvalues of H_{eff}, and hence the poles are symmetrically arranged around the imaginary axis.

The differential conductance $G(V) = dI/dV$ of the quantum dot, measured by grounding the superconduc-
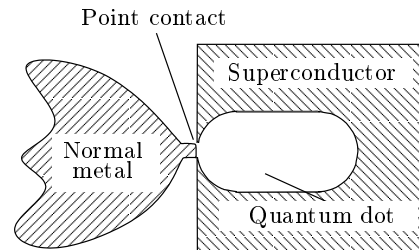
Fig. 2. Schematic illustration of an Andreev billiard

tor and applying a bias voltage to the normal metal, is obtained from the scattering matrix via [7]

$$G(V) = \frac{e^2}{h} \left[\frac{N}{2} - \frac{1}{2} \operatorname{Tr} S(eV)\tau_z S^\dagger(eV)\tau_z\right], \quad (4)$$

in the electron–hole basis, and via

$$G(V) = \frac{e^2}{h} \left[\frac{N}{2} - \frac{1}{2} \operatorname{Tr} S(eV)\tau_y S^\dagger(eV)\tau_y\right], \quad (5)$$

in the Majorana basis. The Pauli matrices τ_y and τ_z act on the electron–hole degree of freedom. The two bases are related by the unitary transformation

$$S \mapsto USU^\dagger, \quad U = \sqrt{\frac{1}{2}} \begin{pmatrix} 1 & 1 \\ i & -i \end{pmatrix}. \quad (6)$$

2.2. Gaussian ensembles

For a random-matrix description, we assume that the scattering in the quantum dot is chaotic, and that this applies to normal scattering from the electrostatic potential as well as to Andreev scattering from the pair potential. In the large-M limit, we can then take a Gaussian distribution for H,

$$P(H) \propto \exp\left(-\frac{c}{M}\operatorname{Tr} H^2\right). \tag{7}$$

By taking the matrix elements of H to be real, complex, or quaternion numbers (in an appropriate basis), one obtains the Wigner–Dyson ensembles of nonsuperconducting chaotic billiards [16–19]. Particle–hole symmetry then plays no role, because normal scattering does not couple electrons and holes.

Altland and Zirnbauer introduced the particle–hole symmetric ensembles appropriate for an Andreev billiard [20]. The two ensembles without time-reversal symmetry are obtained by taking the matrix elements of $i \times H$ (instead of H itself) to be real or quaternion. When iH is real, there is only particle–hole symmetry (class D), while when iH is quaternion, there is particle–hole and spin-rotation symmetry (class C).

Both the Wigner–Dyson (WD) and the Altland–Zirnbauer (AZ) ensembles are characterized by a parameter $\beta \in \{1, 2, 4\}$ that describes the strength of the level repulsion factor in the probability distribution of distinct eigenvalues E_i of H: a factor $\prod_{i<j} |E_i - E_j|^\beta$ in the WD ensembles and a factor $\prod'_{i<j} |E_i^2 - E_j^2|^\beta$ in the AZ ensembles. (The prime indicates that the product includes only the positive eigenvalues.)

In the WD ensembles, the parameter β also counts the number of degrees of freedom of the matrix elements of H: $\beta = 1, 2, 4$ when H is real, complex, or quaternion, respectively. In the AZ ensembles, this connection is lost: $\beta = 2$ in the class C ensemble (iH real) as well as in the class D ensemble (iH quaternion).

The coefficient c can be related to the average spacing δ_0 of distinct eigenvalues of H in the bulk of the spectrum,

$$c = \frac{\beta\pi^2}{8\delta_0^2} \times \begin{cases} 2 & \text{in the WD ensembles,} \\ 1 & \text{in the AZ ensembles.} \end{cases} \tag{8}$$

The coefficient in Eq. (8) for the AZ ensembles is twice as small as it is in the WD ensembles with the same β, on account of the $\pm E$ symmetry of the spectrum (see Appendix A).

Because the distribution of H is basis independent, we can without loss of generality choose a basis such that the coupling matrix W is diagonal,

$$W_{mn} = w_n \delta_{mn}, \quad 1 \le m \le M, \quad 1 \le n \le N. \tag{9}$$

The coupling strength w_n is related to the tunnel probability $\Gamma_n \in (0, 1)$ of mode n into the quantum dot by [14, 15]

$$|w_n|^2 = \frac{M\delta_0}{\pi^2 \Gamma_n}\left(2 - \Gamma_n - 2\sqrt{1 - \Gamma_n}\right). \tag{10}$$

2.3. Class C and D ensembles

We summarize the properties of the $\beta = 2$ AZ ensembles, symmetry class C and D, that we need for our study of the Andreev resonances. (See Appendix B for the corresponding $\beta = 1, 4$ formulas in symmetry classes CI and DIII.) Similar formulas can be found in Ref. [21].

When Andreev scattering operates together with spin-orbit coupling, we can combine electron and hole degrees of freedom from the same spin band into a real basis of Majorana fermions. (This change of basis amounts to the unitary transformation in Eq. (6).) In the Majorana basis, the constraint of particle–hole symmetry is given simply by

$$H = -H^*, \tag{11}$$

and we can therefore take $H = iA$ with A a real antisymmetric matrix. In the Gaussian ensemble, the upper-diagonal matrix elements A_{nm} ($n < m$) all have identical and independent distributions,

$$P(\{A_{nm}\}) \propto \prod_{1=n<m}^{M} \exp\left(-\frac{\pi^2 A_{nm}^2}{2M\delta_0^2}\right) \tag{12}$$

(see Eqs. (7) and (8)). This is the $\beta = 2$ class-D ensemble, without spin-rotation symmetry.

The $\beta = 2$ class-C ensemble applies in the absence of spin-orbit coupling, when spin-rotation symmetry is preserved. Andreev reflection from a spin-singlet superconductor couples only electrons and holes from different spin bands, which cannot be combined into a real basis state. It is then more convenient to stay in the electron–hole basis and to eliminate the spin degree of freedom by considering a single spin band for the electron and the opposite spin band for the hole. (The matrix dimensionality M and the mean level spacing δ_0 then refer to a single spin.) In this basis, the particle–hole symmetry requires that

$$H = -\tau_y H^* \tau_y, \tag{13}$$

where the Pauli matrix τ_y operates on the electron and hole degrees of freedom.

Constraint (13) implies that $H = iQ$ with Q a quaternion anti-Hermitian matrix. Its matrix elements are of the form

$$Q_{nm} = a_{nm}\tau_0 + ib_{nm}\tau_x + ic_{nm}\tau_y + id_{nm}\tau_z, \\ n, m = 1, 2, \dots, M/2, \quad (14)$$

with real coefficients a, b, c, d (to ensure that $Q_{nm} = \tau_y Q_{nm}^* \tau_y$). The anti-Hermiticity of Q requires the off-diagonal elements to be related by $a_{nm} = -a_{mn}$ and $x_{nm} = x_{mn}$ for $x \in \{b, c, d\}$. On the diagonal, $a_{nn} = 0$. In the Gaussian ensemble, the independent matrix elements have the distribution

$$P(\{Q_{nm}\}) \propto \prod_{n=1}^{M/2} \exp\left(-\frac{\pi^2}{2M\delta_0^2}(b_{nn}^2 + c_{nn}^2 + d_{nn}^2)\right) \times$$

$$\times \prod_{1=n<m}^{M/2} \exp\left(-\frac{\pi^2}{M\delta_0^2}(a_{nm}^2 + b_{nm}^2 + c_{nm}^2 + d_{nm}^2)\right). \quad (15)$$

3. ANDREEV RESONANCES

3.1. Accumulation on the imaginary axis

In Fig. 3, we show the location of the poles of the scattering matrix in the complex energy plane, for the $\beta = 2$ AZ ensembles with and without spin-rotation symmetry (class C and D, respectively). The $\beta = 2$ WD ensemble (class A, complex H) is included for comparison. The poles are eigenvalues ε of the non-Hermitian effective Hamiltonian (1), with H distributed according to the Gaussian distribution (7), (8), $\beta = 2$, and the coupling matrix W given by Eqs. (9), (10). For simplicity, we took identical tunnel probabilities $\Gamma_n \equiv \Gamma$ for each of the N modes connecting the quantum dot to the normal metal.

The number M of basis states in the quantum dot is taken much larger than N, to reach the random-matrix regime. In class C, this number is necessarily even, as demanded by the particle–hole symmetry relation (13). The symmetry relation (11) in class D imposes no such constraint, and when M is odd, there is an unpaired Majorana zero mode in the spectrum [21][1]. The class-D superconductor with a Majorana zero mode is

called topologically nontrivial, while a class-C or class-D superconductor without a zero mode is called topologically trivial [22–24]. For a more direct comparison of class C and class D, we take M even in both cases, and hence both superconductors are topologically trivial.

In the absence of particle–hole symmetry (class A), the poles $\varepsilon = E - i\gamma$ of the scattering matrix have the density [25]

$$\rho(E, \gamma) = \frac{N}{4\pi\gamma^2}, \quad \gamma_{min} < \gamma < \gamma_{max}, \quad (16)$$

$$\gamma_{min} = N\Gamma\delta_0/4\pi, \quad \gamma_{max} = \gamma_{min}/(1-\Gamma), \quad (17)$$

for $|E| \ll M\delta_0$ and asymptotically in the limit $N, M/N \to \infty$. For $|E| \gtrsim \delta_0$, all three $\beta = 2$ ensembles A, C, D have a similar density of poles, but for smaller $|E|$, the densities are strikingly different, see Fig. 2. In class C, the poles are repelled from the imaginary axis, but in class D, they accumulate on that axis.

As pointed out in Ref. [12], a nondegenerate pole $\varepsilon = -i\gamma$ on the imaginary axis has a certain stability: it cannot acquire a nonzero real part E without breaking the $\varepsilon \leftrightarrow -\varepsilon^*$ symmetry imposed by particle–hole conjugation. To see why this stability is not operative in class C, we note that on the imaginary axis, γ is a real eigenvalue of the matrix

$$\Omega = -Q + \pi WW^\dagger \quad \text{in class C}, \quad (18)$$

$$\Omega = -A + \pi WW^\dagger \quad \text{in class D}. \quad (19)$$

In both classes, the matrix Ω commutes with an anti-unitary operator, $\mathcal{C}\Omega = \Omega\mathcal{C}$, with $\mathcal{C} = i\tau_y\mathcal{K}$ in class C and $\mathcal{C} = \mathcal{K}$ in class D. (The operator $\mathcal{K}$ performs a complex conjugation.) In class C, this operator $\mathcal{C}$ squares to -1, so a real eigenvalue γ of Ω has a Kramers degeneracy[2] and hence nondegenerate poles $\varepsilon = -i\gamma$ on the imaginary axis are forbidden. In class D, in contrast, the operator $\mathcal{C}$ squares to $+1$, Kramers degeneracy is inoperative, and nondegenerate poles are allowed and in fact generic.

3.2. Square-root law

As we explain in Appendix C, for ballistic coupling ($\Gamma = 1$), the statistics of poles on the imaginary axis can be mapped onto the statistics of the real eigenvalues of an $M \times M$ random orthogonal matrix with N rows and

---

[1] Since Majorana zero modes always appear in pairs, the change from M even to M odd necessarily involves some external system that can absorb one of the two modes. For example, this could be a nanowire coupled at one end to the quantum dot, such that the Majorana zero mode inside the quantum dot is paired with the zero mode at the other end of the wire. At the transition from M odd to even, the two Majorana modes merge because the gap in the nanowire closes.

[2] The usual Kramers degeneracy refers to the eigenvalues of a Hermitian matrix that commutes with an anti-unitary operator squaring to -1. Here the matrix is not Hermitian, but the degeneracy still applies to real eigenvalues.
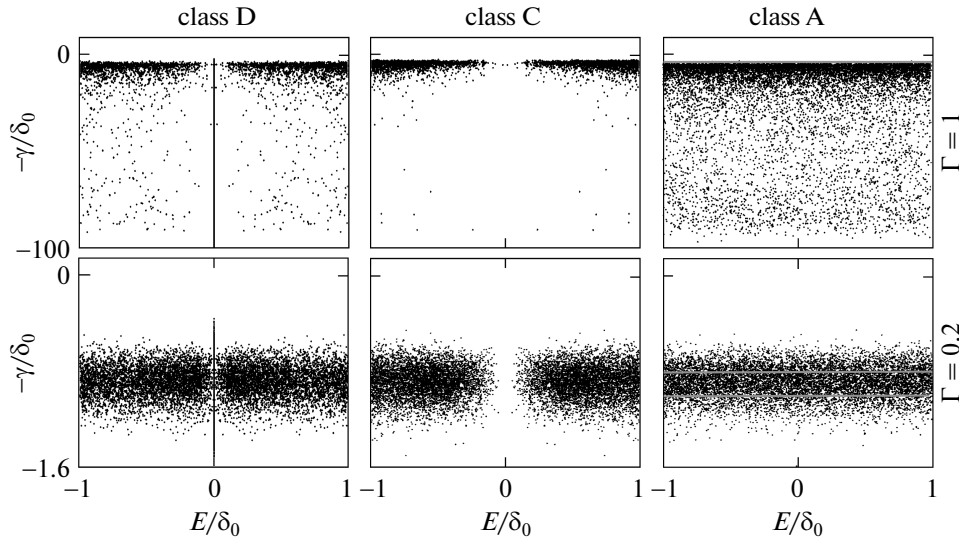
Fig. 3. Scatter plot of the poles $\varepsilon = E - i\Gamma$ of 5000 scattering matrices $S(\varepsilon)$, in the Gaussian ensembles of class D, C, and A (first, second, and third column), for ballistic coupling ($\Gamma = 1$, first row) and for tunnel coupling ($\Gamma = 0.2$, second row). In each case, the Hamiltonian has dimension $M \times M = 500 \times 500$ and the scattering matrix, $N \times N = 50 \times 50$. Only a narrow energy range near $E = 0$ is shown, to contrast the accumulation of poles on the imaginary axis in class D and the repulsion in class C. The horizontal lines indicate the expected boundaries (17) of the class-A scatter plot in the limit $N, M/N \to \infty$

columns deleted; this is a solved problem [26, 27]. The linear density profile $\rho_0(\gamma)$ on the imaginary axis is

$$\rho_0(\gamma) = \sqrt{\frac{N\Gamma}{8\pi}}\, \frac{1}{\gamma}, \quad \gamma_{min} < \gamma < \gamma_{max}, \qquad (20)$$
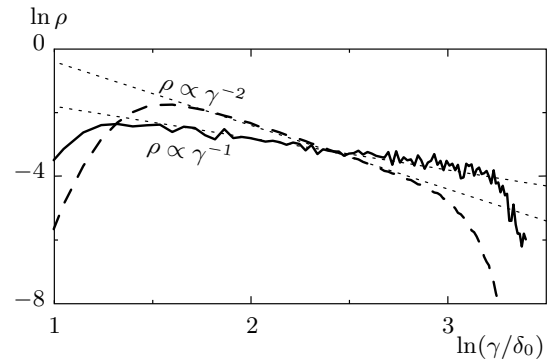
for $1 \ll N\Gamma \ll M$ and γ_{min}, γ_{max} given by Eq. (17). We conjecture that this density profile, derived [26] for $\Gamma = 1$, holds also for $\Gamma < 1$. In Fig. 4, we give numerical evidence in support of this conjecture.

In Fig. 5, we show how the average number $\langle N_Y \rangle$ of class-D poles on the imaginary axis depends on the dimensionality N of the scattering matrix and on the tunnel probability Γ. We compare with the square-root law[3)]

$$\langle N_Y \rangle = -\sqrt{\frac{N\Gamma}{8\pi}} \ln(1 - \Gamma) \qquad (21)$$

implied by integration of our conjectured density profile (20). This $\sqrt{N}$ scaling is generic for random-matrix ensembles that exhibit accumulation of eigenvalues on the real or imaginary axis, such as the Ginibre ensemble [28–30] (real Gaussian matrices without any sym-


Fig. 4. Double-logarithmic plot of the probability distribution $\rho(\gamma)$, normalized to unity, of the imaginary part γ of the poles of the scattering matrix. The curves are calculated by averaging over some 2000 realizations of the class-D ensemble, with $N = 10$, $M = 500$, $\Gamma = 0.9$. The dashed curve includes all poles, while the blue solid curve includes only the poles on the imaginary axis ($E = 0$). The black dotted lines are the predicted slopes from Eq. (16) and (20)

metry) and the Hamilton ensemble [31][4)] (matrices of

[3)] The logarithmic divergence in Eq. (21) for $\Gamma = 1$ is cut-off by the finite dimension M of the Hamiltonian, such that $\langle N_Y \rangle \approx$ $\approx N^{1/2} \ln(M/N)$ for ballistic coupling. This spurious M-dependence does not exist for $\Gamma < 1$.

[4)] The supplement to this paper (an appendix in arXiv: 1305.2924) contains an overview of the square-root law in a variety of random-matrix ensembles.
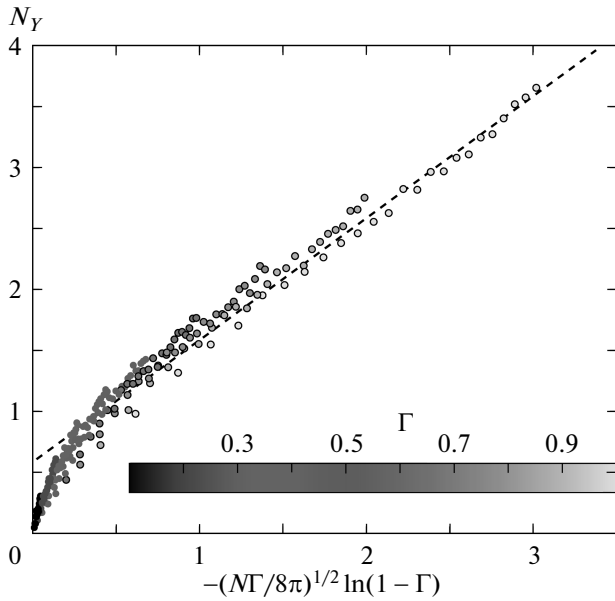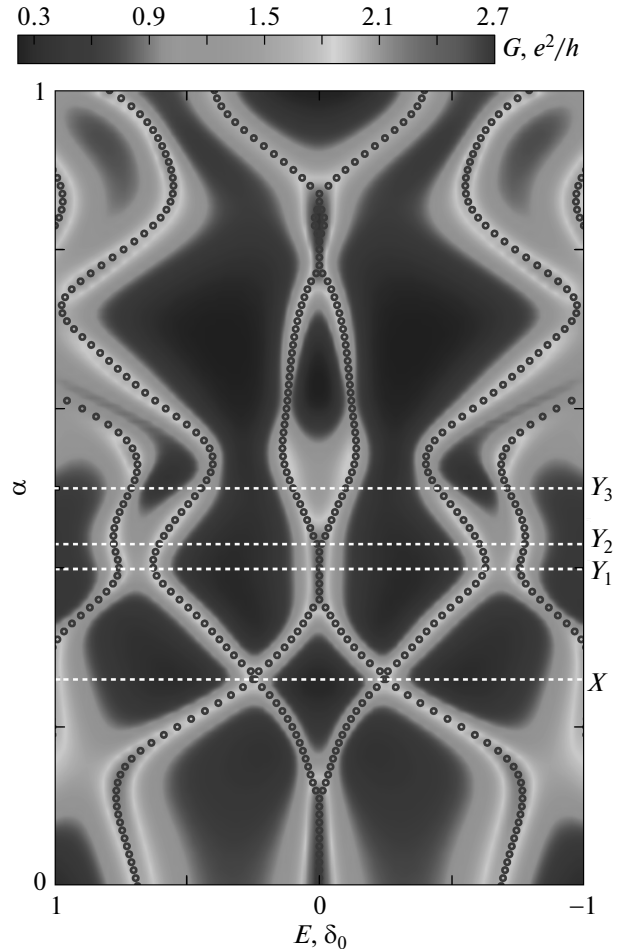
Fig. 5. Average of the number N_Y of poles on the imaginary axis for an $N \times N$ scattering matrix $S(\varepsilon)$ in symmetry class D. Degree of grey distinguishes different tunnel couplings $\Gamma < 1$, and N is increased together with $M = 80N$. The slope of the dashed line is the large-N asymptote (21)
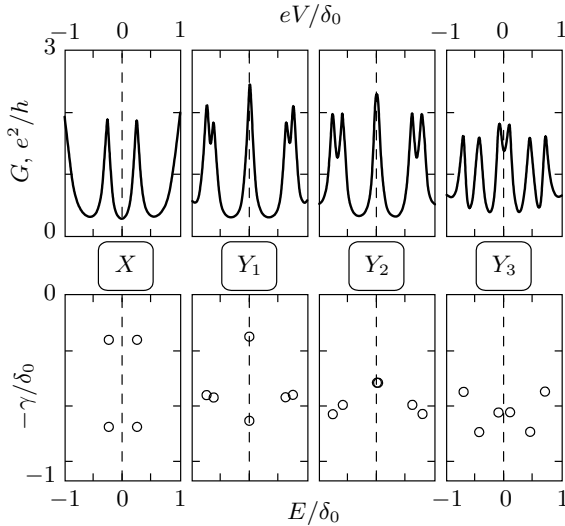

Fig. 6. Parametric evolution of the differential conductance $G(V, \alpha)$ (grey scale) and the real part E of the poles of the scattering matrix $S_\alpha(\varepsilon)$. These are results for a single realization of the class D ensemble with $M = 120$, $N = 6$, and $\Gamma = 0.3$

the form $\mathcal{M} = HJ$ with H a symmetric real Gaussian matrix and $J = \begin{pmatrix} 0 & 1 \\ -1 & 0 \end{pmatrix}$ a fixed anti-symmetric matrix). Figure 5 shows that the Andreev resonances follow the same square-root law.

4. X-SHAPED AND Y-SHAPED CONDUCTANCE PROFILES

In Ref. [7], it was found in a computer simulation of a superconducting InSb nanowire that the conductance resonances trace out two distinct profiles in the voltage–magnetic-field plane: an X-shape or a Y-shape. In the X-shaped profile, a pair of conductance resonances merges and immediately splits again upon variation of the voltage V or magnetic field B. In the Y-shaped profile, a pair of peaks merges at $V = 0$ and then stays pinned to zero voltage over a range of magnetic field values. Here, we wish to relate this phenomenology to the parametric evolution of poles of the scattering matrix in the complex energy plane [12].

For that purpose, we introduce a parameter depen-

dence in the Hamiltonian H of the Andreev billiard,

$$H_\alpha = (1 - \alpha)H_0 + \alpha H_1, \qquad (22)$$

and calculate the differential conductance as a function of V and α. We work in symmetry class D (broken time-reversal and broken spin-rotation symmetry), and hence H_0 and H_1 are purely imaginary antisymmetric matrices (in the Majorana basis). We draw them from the Gaussian distribution (12). The scattering matrix S_α, obtained from H_α via Eq. (2), gives the differential conductance $G(V, \alpha)$ via Eq. (5). For each α, we also compute the poles $\varepsilon = E - i\gamma$ of $S(\varepsilon)$ in the complex energy plane.

Figure 6 shows a typical realization where the num-

Fig. 7. Four cuts through the parametric evolution in Fig. 6, showing the differential conductance $G = dI/dV$ (top row) and scattering matrix poles $\varepsilon = E - i\gamma$ (bottom row)

ber N_Y of conductance poles on the imaginary axis switches between zero and two as α varies in the interval $[0, 1]$. The color-scale plot shows $G(V, \alpha)$, while the dots trace out the projection of the poles of $S_\alpha(\varepsilon)$ on the real axis. Labels X and Y indicate the two types of profiles, and Fig. 7 shows the corresponding conductance peaks and scattering matrix poles.

Inspection of the figures shows that the X-shaped profile appears when two scattering matrix poles cross when projected onto the real axis. (They do not cross in the complex energy plane.) The Y-shaped profile appears when N_Y jumps by two.

5. CONCLUSION

For a closed superconducting quantum dot, the distinction between topologically trivial and nontrivial is the absence or presence of a level pinned to the middle of the gap (a Majorana zero mode). When the quantum dot is connected to a metallic reservoir, the bound states become quasi-bound, $E \mapsto E - i\gamma$, with a finite lifetime $\hbar/2\gamma$. The distinction between topologically trivial and nontrivial then reduces to whether the number N_Y of quasi-bound states with $E = 0$ is even or odd.

Two types of transitions can be distinguished [12]: At a topological phase transition, N_Y changes by ± 1 (see footnote 1)). At a "pole transition", N_Y changes by ± 2. Both types of transitions produce the same

Y-shaped conductance profile of two peaks that merge and stick together for a range of parameter values — distinct from the X-shaped profile that occurs without a change in N_Y.

There is a variety of methods to distinguish the pole transition from the topological phase transition [7]: since $N_Y \approx \Gamma^{3/2}\sqrt{N}$ for $\Gamma \ll 1$, one way to suppress the pole transitions is to couple the metal to the superconductor via a small number of modes N with a small transmission probability Γ. The pole transitions are a sample-specific effect, while the topological phase transition is expected to be less sensitive to microscopic details of the disorder. We do not therefore expect the pole transitions to reproduce in the same sample upon thermal cycling. If we can measure from both ends of a nanowire, we might search for correlations between the conductance peaks at the two ends. The Majorana zero modes come in pairs, one at each end, and hence there should be a correlation in the conductance peaks measured at the two ends, which we would not expect to be there for the peaks due to the pole transition.

APPENDIX A

Factor-of-two difference in the construction of Gaussian ensembles with or without particle–hole symmetry

As we discussed in Sec. 2.2, in the Gaussian ensembles of random-matrix theory, the Hermitian $M \times M$ matrix H has the distribution

$$P(H) \propto \exp\left(-\frac{c}{M}\operatorname{Tr}H^2\right), \qquad \text{(A.1a)}$$

$$c = \frac{\beta\pi^2}{8\delta_0^2} \times \begin{cases} 2 & \text{in the WD ensembles,} \\ 1 & \text{in the AZ ensembles,} \\ 1 & \text{in the chiral ensembles.} \end{cases} \qquad \text{(A.1b)}$$

In each ensemble, δ_0 refers to the average spacing of distinct eigenvalues of H in the bulk of the spectrum. For $\beta = 4$, the eigenvalues have a twofold Kramers degeneracy, so there are only $M_0 = M/2$ distinct eigenvalues, while for $\beta = 1, 2$, all the $M_0 = M$ eigenvalues are distinct (disregarding spin degeneracy).

We have experienced that the factor-of-two difference in the coefficient between the WD and AZ ensem-

bles is a source of confusion. Here, we hope to resolve this confusion by pointing to its origin, which is the $\pm E$ symmetry of the spectrum in the AZ ensembles (and also in the chiral ensembles, which we include for completeness). The calculation of the coefficient c is a bit lengthy, with factors of two appearing at different places before the final factor remains, but we have not found a much shorter and convincing argument for the difference.

The eigenvalue distribution in the WD ensembles is [16–18]

$$
P(E_1, E_2, \ldots, E_{M_0}) \propto
$$
$$
\propto \prod_{1=i<j}^{M_0} |E_i - E_j|^\beta \prod_{k=1}^{M_0} e^{-\frac{c}{M_0}E_k^2}, \quad (A.2)
$$

where the indices i, j, k range over the M_0 distinct eigenvalues.

In the AZ ensembles, an eigenvalue at $+E$ has a partner at $-E$, which is a distinct eigenvalue if $E \neq 0$. For the average level spacing in the bulk of the spectrum, the existence of a level pinned at $E = 0$ is irrelevant, and we therefore assume that there are no such zero modes. (This requires M_0 even.) The eigenvalue distribution then has the form [20, 21]

$$
P(E_1, E_2, \ldots, E_{M_0/2}) \propto \prod_{1=i<j}^{M_0/2} |E_i^2 - E_j^2|^\beta \times
$$
$$
\times \prod_{k=1}^{M_0/2} |E_k|^\alpha \exp\left(-\frac{2c}{M_0}E_k^2\right), \quad (A.3)
$$

where the indices i, j, k now range only over the $M_0/2$ distinct positive eigenvalues. There is a new exponent $\alpha \in \{0, 1, 2\}$ that governs the repulsion between eigenvalues related by the $\pm E$ symmetry. This factor $|E_k|^\alpha$ only affects the first few levels around $E = 0$, and we can therefore ignore it for a calculation of the average level spacing in the bulk of the spectrum, effectively setting $\alpha \to 0$.

The two distributions (A.2) and (A.3) can be written in the same form with the help of the microscopic level density

$$
\rho(E) = \sum_{n=1}^{M_0} \delta(E - E_n), \quad (A.4)
$$

defined for each set of M_0 distinct energy levels. At the mean-field level, sufficient for a calculation of the density of states in the large-M limit, we can assume that $\rho(E)$ is a smooth function of E (Coulomb gas model [16]).

The eigenvalue distribution has the form of a Gibbs distribution $P \propto \exp(-\beta U)$, with the energy functional

$$
U_{WD} = -\frac{1}{2} \int_{-\infty}^{\infty} dE \int_{-\infty}^{\infty} dE' \, \rho(E)\rho(E') \ln|E - E'| +
$$
$$
+ \frac{c}{\beta M_0} \int_{-\infty}^{\infty} dE \, E^2 \rho(E) \quad (A.5)
$$

for the WD ensembles and

$$
U_{AZ} = -\frac{1}{2} \int_{0}^{\infty} dE \int_{0}^{\infty} dE' \, \rho(E)\rho(E') \ln|E^2 - E'^2| +
$$
$$
+ \frac{2c}{\beta M_0} \int_{0}^{\infty} dE \, E^2 \rho(E) =
$$
$$
= -\frac{1}{4} \int_{-\infty}^{\infty} dE \int_{\infty}^{\infty} dE' \, \rho(E)\rho(E') \ln|E - E'| +
$$
$$
+ \frac{c}{\beta M_0} \int_{-\infty}^{\infty} dE \, E^2 \rho(E), \quad (A.6)
$$

for the AZ ensembles (at $\alpha = 0$). In the second equality, we used the $\pm E$ symmetry $\rho(E) = \rho(-E)$.

The mean-field density of states $\bar{\rho}(E)$ minimizes U with the normalization constraint

$$
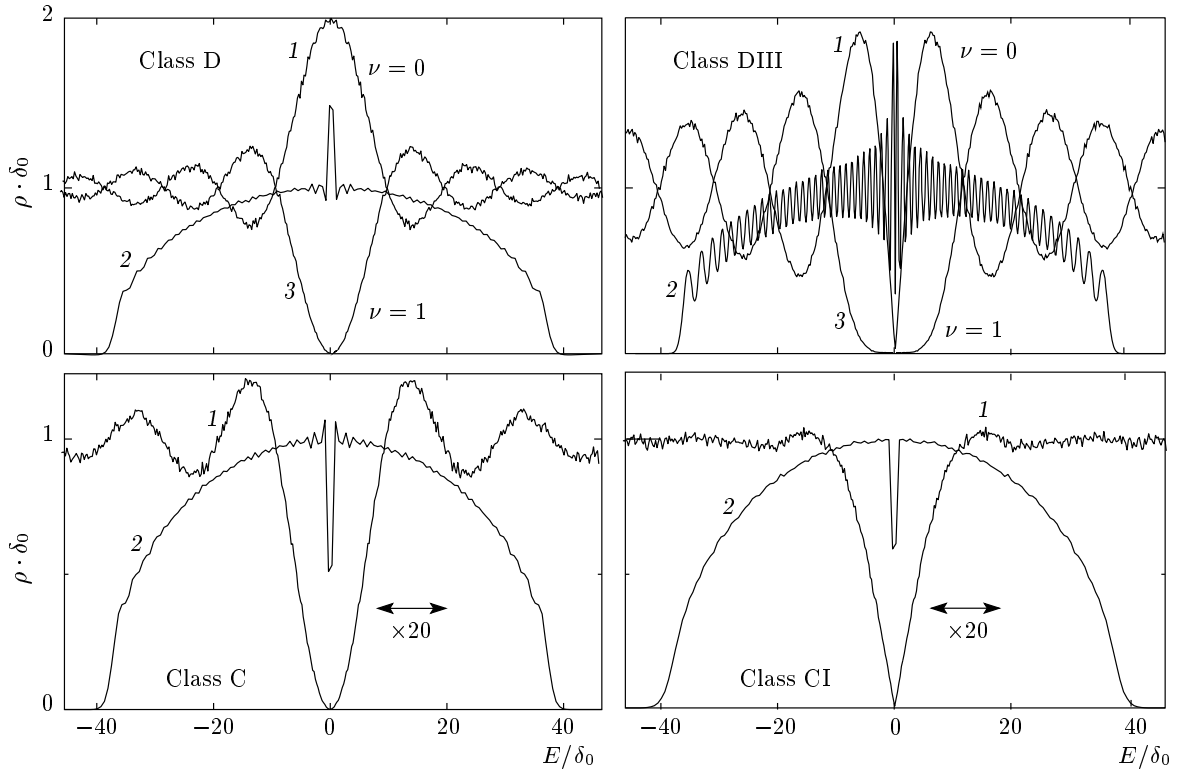\int_{-\infty}^{\infty} dE \, \bar{\rho}(E) = M_0. \quad (A.7)
$$

The normalization constraint is the same in the WD and AZ ensembles, but the minimization condition is different:

$$
\frac{\delta U_{WD}}{\delta \rho(E)} = 0 \Rightarrow -\int_{-\infty}^{\infty} dE' \, \bar{\rho}_{WD}(E') \ln|E - E'| +
$$
$$
+ \frac{c}{\beta M_0} E^2 = \text{const}, \quad (A.8)
$$

$$
\frac{\delta U_{AZ}}{\delta \rho(E)} = 0 \Rightarrow -\frac{1}{2} \int_{-\infty}^{\infty} dE' \, \bar{\rho}_{AZ}(E') \ln|E - E'| +
$$
$$
+ \frac{c}{\beta M_0} E^2 = \text{const}. \quad (A.9)
$$

The $\pm E$ symmetry does not introduce an additional constraint on $\bar{\rho}_{AZ}(E)$, since Eq. (A.9) automatically produces an even density.

Fig. 8. Curves *1*, *2*: average density of states in the four AZ ensembles, calculated numerically for Hamiltonians of dimension $M \times M = 60 \times 60$ in classes C, CI, and D and $M \times M = 120 \times 120$ in class DIII (when each level has a twofold Kramers degeneracy; ρ and δ_0 refer to distinct levels). Curve *1* shows the full semicircle, curve *2* shows the region around $E = 0$ (horizontally enlarged by a factor of 20). These are all results for a topologically trivial superconductor, without a zero mode ($\nu = 0$). Curves *3* (labeled $\nu = 1$) show the effect of a zero mode in class D ($M = 61$) and class DIII ($M = 122$). The delta-function peak from the zero mode itself is not plotted

The solution of this integral equation gives the familiar semi-circular density of states [16]

$$\bar{\rho}_{WD}(E) = \frac{2c}{\pi\beta M_0}\sqrt{\frac{\beta}{c}M_0^2 - E^2}, \qquad (A.10)$$

$$\bar{\rho}_{AZ}(E) = \frac{4c}{\pi\beta M_0}\sqrt{\frac{\beta}{2c}M_0^2 - E^2}. \qquad (A.11)$$

The mean level spacing near $E = 0$ is $\delta_0 = 1/\bar{\rho}(0)$, leading to

$$\delta_0 = \begin{cases} \dfrac{1}{2}\pi\sqrt{\beta/c} & \text{in the WD ensembles,} \\[2mm] \dfrac{1}{2}\pi\sqrt{\beta/2c} & \text{in the AZ ensembles,} \end{cases} \qquad (A.12)$$

which amounts to Eq. (A.1b). We note that the additional factor-of-two arises solely from the $\pm E$ symmetry of the spectrum, and it is therefore irrelevant whether this is a consequence of particle–hole symmetry or of chiral symmetry.

To check that we have not missed a factor of two, in Fig. 8, we show the numerical result of averaging over a large number of random Hamiltonians in each of the four AZ ensembles. The semi-circular density of states (A.11) applies away from the band center, with the expected limit $\rho \times \delta_0 \to 1$ near $E = 0$.

In Fig. 8, we also see the anomalies at band center that we ignored in our calculation. Without a zero mode ($\nu = 0$), the density of states vanishes as $|E|^\alpha$ with $\alpha = 2$ in class C and $\alpha = 1$ in class CI and DIII [20]. In class D, we have $\alpha = 0$, which means that the $\pm E$ pairs of energy levels do not repel at the band center. The density of states then has a quadratic peak at $E = 0$. The delta-function peak of a zero mode has also an effect on the smooth part of the density of states, which for $\nu = 1$ vanishes as $|E|^{\alpha+\beta}$, as E^2 in class D, and as $|E|^5$ in class DIII [21].

APPENDIX B

Altland–Zirnbauer ensembles with time-reversal symmetry

For completeness and reference, we record the $\beta = 1, 4$ counterparts of the $\beta = 2$ formulas (12) and (15). These are the AZ symmetry classes CI ($\beta = 1$, time-reversal with spin-rotation symmetry) and DIII ($\beta = 4$, time-reversal without spin-rotation symmetry) [20]. The time-reversal symmetry conditions on the Hamiltonian matrix are

$$H = H^* \text{ for } \beta = 1,$$
$$H = \sigma_y H^* \sigma_y \text{ for } \beta = 4. \qquad (B.1)$$

The Pauli matrix σ_y acts on the spin degree of freedom: the Pauli matrices τ_i we used previously acted on the electron-hole degree of freedom.

A compact representation can be given if we use the electron–hole basis for $\beta = 1$ and the Majorana basis for $\beta = 4$. The matrix elements of the Hamiltonian can then be represented by Pauli matrices:

$$H_{nm} = a_{nm}\tau_x + b_{nm}\tau_z \text{ for } \beta = 1,$$
$$H_{nm} = ic_{nm}\sigma_x + id_{nm}\sigma_z \text{ for } \beta = 4, \qquad (B.2)$$

with real coefficients a, b, c, d. We note that iH for $\beta = 1$ is quaternion, and hence this class CI ensemble is a subset of the class C ensemble. Similarly, because iH is real for $\beta = 4$, this class DIII ensemble is a subset of class D.

The Hermiticity of H requires that the off-diagonal elements are related by $a_{nm} = a_{mn}$, $b_{nm} = b_{mn}$, $c_{nm} = -c_{mn}$, and $d_{nm} = -d_{mn}$. On the diagonal, $c_{nn} = d_{nn} = 0$. The indices n, m range from 1 to $M/2$, for an $M \times M$ matrix H. (The dimensionality is necessarily even to accomodate the Pauli matrices.) For $\beta = 4$, there is a twofold Kramers degeneracy of the energy levels, and therefore only $M/2$ eigenvalues of H are distinct. For $\beta = 1$, all M eigenvalues are distinct (the spin degeneracy that exists in class C, CI is not included in M). The mean level spacing δ_0 refers to the distinct eigenvalues.

Combining Eq. (B.2) with Eqs. (7) and (8) gives the probability distribution of the independent matrix elements in the Gaussian ensemble:

$$P(\{H_{nm}\}) \propto \prod_{n=1}^{M/2} \exp\left(-\frac{\pi^2}{4M\delta_0^2}(a_{nn}^2 + b_{nn}^2)\right) \times$$
$$\times \prod_{1=n<m}^{M/2} \exp\left(-\frac{\pi^2}{2M\delta_0^2}(a_{nm}^2 + b_{nm}^2)\right) \quad (B.3)$$

for $\beta = 1$, class CI, and

$$P(\{H_{nm}\}) \propto \prod_{1=n<m}^{M/2} \times$$
$$\times \exp\left(-\frac{2\pi^2}{M\delta_0^2}(c_{nm}^2 + d_{nm}^2)\right) \quad (B.4)$$

for $\beta = 4$, class DIII.

APPENDIX C

Mapping of the pole statistics problem onto the eigenvalue statistics problem of truncated orthogonal matrices

We show how the result in Eq. (20) for the density profile of imaginary poles of the scattering matrix follows from the known distribution of real eigenvalues of truncated orthogonal matrices [26], in the case $\Gamma = 1$ of ballistic coupling.

Following Refs. [32, 33], we construct the $N \times N$ energy-dependent unitary scattering matrix $S(E)$ in terms of an $M \times M$ energy-independent orthogonal matrix O,

$$S(E) = \mathcal{P}O(e^{-2\pi iE/M\delta_0} + \mathcal{R}O)^{-1}\mathcal{P}^T. \qquad (C.1)$$

The rectangular $N \times M$ matrix $\mathcal{P}$ has elements $\mathcal{P}_{nm} = \delta_{nm}$ and $\mathcal{R} = 1 - \mathcal{P}^T\mathcal{P}$. The $M \times M$ Hermitian matrix H is related to O via a Cayley transform,

$$O = \frac{\pi H/M\delta_0 + i}{\pi H/M\delta_0 - i} \Leftrightarrow H = \frac{iM\delta_0}{\pi}\frac{O+1}{O-1}. \qquad (C.2)$$

Equation (C.2) with O uniformly distributed according to the Haar measure in $SO(N)$ produces the Gaussian distribution (7) for H, in the low-energy range $|E| \lesssim N\delta_0 \ll M\delta_0$. Furthermore, in this low-energy range, scattering matrix (C.1) is related to H by Eq. (2) with the ballistic coupling matrix $W = \mathcal{P}^T(M\delta_0/\pi^2)^{1/2}$.

A pole $\varepsilon = -i\gamma$ of $S(\varepsilon)$ on the imaginary axis corresponds to a real eigenvalue

$$x = e^{-2\pi\gamma/M\delta_0} \qquad (C.3)$$

of the $(M-N) \times (M-N)$ matrix $\tilde{O} = \mathcal{R}O\mathcal{R}$ obtained from the orthogonal matrix O by deleting the first N rows and columns. For $M \gg 1$, the x-dependent density $\tilde{\rho}_0(x)$ is given by [26]

$$\tilde{\rho}_0(x) = \frac{1}{B(N/2, 1/2)}\frac{1}{1-x^2}, \quad x^2 < 1 - N/M, \quad (C.4)$$

with $B(a, b)$ being the beta function.

Using Eq. (C.3), we thus arrive for $N \ll M$ at the γ-dependent density

$$\rho_0(\gamma) = \frac{1}{B(N/2, 1/2)} \frac{1}{2\gamma}, \quad \gamma > N\delta_0/4\pi. \quad (C.5)$$

Equation (20) with $\Gamma = 1$ results if we also assume that $N \gg 1$, such that we can approximate $B(N/2, 1/2) \approx \approx (2\pi/N)^{1/2}$.

REFERENCES

1. A. F. Andreev, Zh. Eksp. Teor. Fiz. **46**, 1823 (1964) [Sov. Phys. JETP **19**, 1228 (1964)].

2. M. Silaev and G. E. Volovik, arXiv:1405.1007, Zh. Eksp. Teor. Fiz. **146**, 12 (2014).

3. J. Alicea, Rep. Progr. Phys. **75**, 076501 (2012).

4. M. Leijnse and K. Flensberg, Semicond. Sci. Technol. **27**, 124003 (2012).

5. T. D. Stanescu and S. Tewari, J. Phys. Condens. Matter **25**, 233201 (2013).

6. C. W. J. Beenakker, Annu. Rev. Con. Mat. Phys. **4**, 113 (2013).

7. D. I. Pikulin, J. P. Dahlhaus, M. Wimmer, H. Schomerus, and C. W. J. Beenakker, New J. Phys. **14**, 125011 (2012).

8. P. W. Brouwer and C. W. J. Beenakker, Phys. Rev. B **52**, 3868 (1995).

9. A. Altland and M. R. Zirnbauer, Phys. Rev. Lett. **76**, 3420 (1996).

10. P. A. Ioselevich, P. M. Ostrovsky, and M. V. Feigel'man, Phys. Rev. B **86**, 035441 (2012).

11. D. Bagrets and A. Altland, Phys. Rev. Lett. **109**, 227005 (2012).

12. D. I. Pikulin and Yu. V. Nazarov, JETP Lett. **94**, 693 (2011); Phys. Rev. B **87**, 235421 (2013).

13. C. W. J. Beenakker, Lect. Notes Phys. **667**, 131 (2005); arXiv:cond-mat/0406018.

14. T. Guhr, A. Müller-Groeling, and H. A. Weidenmüller, Phys. Rep. **299**, 189 (1998).

15. C. W. J. Beenakker, Rev. Mod. Phys. **69**, 731 (1997).

16. M. L. Mehta, *Random Matrices*, Elsevier, Amsterdam (2004).

17. P. J. Forrester, *Log-Gases and Random Matrices*, Princeton University Press (2010).

18. *The Oxford Handbook of Random Matrix Theory*, ed. by G. Akemann, J. Baik, and P. Di Francesco, Oxford University Press, Oxford (2011);

19. Y. V. Fyodorov and D. V. Savin, arXiv:1003.0702; M. R. Zirnbauer, arXiv:1001.0722; C. W. J. Beenakker, arXiv:0904.1432.

20. A. Altland and M. R. Zirnbauer, Phys. Rev. B **55**, 1142 (1997).

21. D. A. Ivanov, J. Math. Phys. **43**, 126 (2002).

22. S. Ryu, A. P. Schnyder, A. Furusaki, and A. W. W. Ludwig, New J. Phys. **12**, 065010 (2010).

23. M. Z. Hasan and C. L. Kane, Rev. Mod. Phys. **82**, 3045 (2010).

24. X.-L. Qi and S.-C. Zhang, Rev. Mod. Phys. **83**, 1057 (2011).

25. Y. V. Fyodorov and H.-J. Sommers, J. Math. Phys. **38**, 1918 (1997).

26. B. A. Khoruzhenko, H.-J. Sommers, and K. Zyczkowski, Phys. Rev. E **82**, 040106(R) (2010).

27. P. J. Forrester, J. Stat. Mech. P12018 (2010).

28. J. Ginibre, J. Math. Phys. **6**, 440 (1965).

29. N. Lehmann and H.-J. Sommers, Phys. Rev. Lett. **67**, 2403 (1991).

30. A. Edelman, E. Kostlan, and M. Shub, J. Amer. Math. Soc. **7**, 247 (1994); A. Edelman, J. Multivariate Anal. **60**, 203 (1997).

31. C. W. J. Beenakker, J. M. Edge, J. P. Dahlhaus, D. I. Pikulin, S. Mi, and M. Wimmer, Phys. Rev. Lett. **111**, 037001 (2013).

32. P. W. Brouwer, K. M. Frahm, and C. W. J. Beenakker, Waves in Random Media **9**, 91 (1999).

33. M. Marciani, P. W. Brouwer, and C. W. J. Beenakker, Phys. Rev. B **90**, 045403 (2014).